

HENet++: Hybrid Encoding and Multi-task Learning for 3D Perception and End-to-end Autonomous Driving

Zhongyu Xia¹, Zhiwei Lin¹, Yongtao Wang^{1*}, Ming-Hsuan Yang²

¹Wangxuan Institute of Computer Technology, Peking University, Beijing, China.

²University of California, Merced, USA.

*Corresponding author(s). E-mail(s): wyt@pku.edu.cn;

Contributing authors: xiazhongyu@pku.edu.cn; zwlin@pku.edu.cn; mhyang@ucmerced.edu;

Abstract

Three-dimensional feature extraction is a critical component of autonomous driving systems, where perception tasks such as 3D object detection, bird’s-eye-view (BEV) semantic segmentation, and occupancy prediction serve as important constraints on 3D features. While large image encoders, high-resolution images, and long-term temporal inputs can significantly enhance feature quality and deliver remarkable performance gains, these techniques are often incompatible in both training and inference due to computational resource constraints. Moreover, different tasks favor distinct feature representations, making it difficult for a single model to perform end-to-end inference across multiple tasks while maintaining accuracy comparable to that of single-task models. To alleviate these issues, we present the HENet and HENet++ framework for multi-task 3D perception and end-to-end autonomous driving. Specifically, we propose a hybrid image encoding network that uses a large image encoder for short-term frames and a small one for long-term frames. Furthermore, our framework simultaneously extracts both dense and sparse features, providing more suitable representations for different tasks, reducing cumulative errors, and delivering more comprehensive information to the planning module. The proposed architecture maintains compatibility with various existing 3D feature extraction methods and supports multimodal inputs. HENet++ achieves state-of-the-art end-to-end multi-task 3D perception results on the nuScenes benchmark, while also attaining the lowest collision rate on the nuScenes end-to-end autonomous driving benchmark.

Keywords: Autonomous Driving, 3D Object Detection, BEV Segmentation, Occupancy Network, 3D Perception

1 Introduction

3D perception capability is the foundation of autonomous driving systems and various other embodied control systems. It is responsible for encoding sensor information, extracting and interpreting features, and serves as a prerequisite for an agent’s interaction with the world. Specifically, 3D perception encompasses tasks such as 3D object

detection, Bird’s Eye View (BEV) semantic segmentation, and semantic occupancy prediction. Some autonomous driving systems are divided into multiple deep learning modules, where the results of 3D perception are used for subsequent planning and control. In recent years, end-to-end autonomous driving has gained increasing attention. This approach employs a single network that

takes sensor information as input and directly outputs trajectory planning or control commands for the ego vehicle. This does not bypass perception because 3D feature extraction from sensor information remains indispensable. Moreover, many studies [1–3] have pointed out that relying solely on trajectory supervision makes it difficult for the network to learn complex logic, leading to hallucinations. Therefore, the model still requires perceptual task decoders to impose constraints on the 3D features.

In the process of building an end-to-end autonomous driving system, there are several challenges. The first challenge is the difficulty in simultaneously achieving higher resolution, larger encoding networks, and more frames. Autonomous driving requires recognizing objects tens or even hundreds of meters away, which necessitates the use of high-resolution multi-view images. Processing high-resolution images often requires an encoder with larger parameter sizes and computational demands (including backbones, necks, depth network or Transformers for 2D-to-3D transformation, etc.). Additionally, given the limited overlap between multi-camera images, stereo spatial information often relies on temporal sequences. Moreover, information about occluded objects must also be retrieved from historical frames. However, each of these aspects requires more computational resources, thereby increasing training costs.

The second challenge is multi-task learning. The vast majority of existing 3D perception work is single-task. Even those claiming multi-task compatibility often train a separate model for each task. However, in 3D perception models, over 80% of the computational load is concentrated in the sensor information encoding part. A single model predicting multiple tasks end-to-end can save computational resources. Yet, some tasks focus on foreground objects while others concentrate on background elements, potentially favoring different model architectures. When sharing an encoder directly, the predictive performance on each task tends to be lower than with single-task models. Additionally, loading pre-trained parameters from different tasks can also affect the performance of each task. How to balance these tasks and enhance their overall performance remains a question worthy of research.

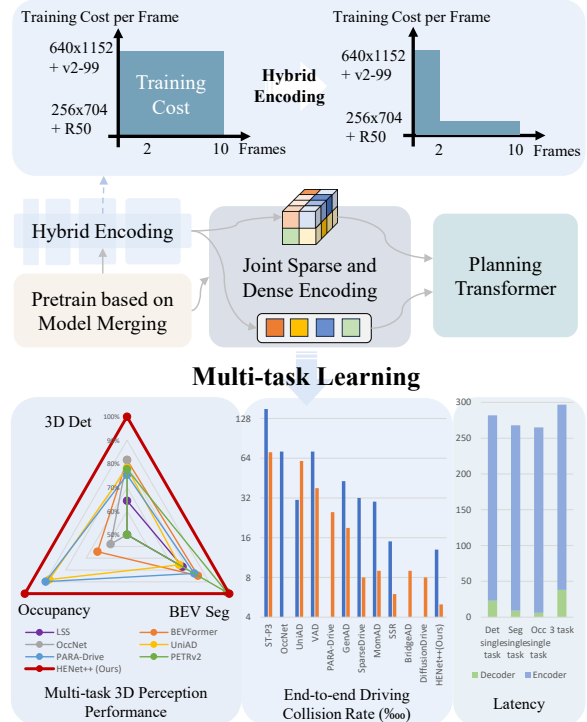


Fig. 1: HENet++ reduces the training cost of simultaneously using high-resolution images and long-sequence temporal data via Hybrid Encoding. By integrating Hybrid Encoding, Joint Sparse and Dense Encoding, and Pretrain based on Model Merging, HENet++ achieves state-of-the-art multi-task performance while attaining the lowest end-to-end driving collision rate on nuScenes.

The third challenge is how to fully leverage multi-modal information and the capabilities of advanced 3D perception models to build end-to-end autonomous driving systems. Current end-to-end autonomous driving approaches utilize different subtask outcomes, employ diverse 3D representations, and design varied planning modules, resulting in a considerable number of complex designs. However, no unified paradigm has yet been established. Meanwhile, most of these works rely solely on visual sensors, while millimeter-wave Radar has gradually become a mainstream configuration for intelligent vehicles in recent years due to its low cost and ability to provide 3D positioning and object velocity information. Developing end-to-end autonomous driving systems that incorporate millimeter-wave Radar is also a promising research direction.

To address the aforementioned challenges, we propose the HENet++ series. To address the first challenge, we introduce Hybrid Encoding, which utilizes a large neural network to encode a small number of high-resolution frames and a compact neural network to process long-sequence low-resolution frames. This approach achieves the advantages of both high resolution and long temporal coverage at a relatively low computational cost. Through further development, our proposed Hybrid Encoding is applicable to both dense (e.g., BEV and voxel) and sparse feature extraction, making it compatible with various existing 3D feature extraction methods. For the second challenge, we propose a multi-task BEV feature encoding specifically designed for BEV models. We further analyze the preferences of different tasks and simultaneously extract both sparse and dense features—providing sparse features for sparse tasks (e.g., 3D object detection) and voxel features for dense tasks (e.g., BEV semantic segmentation or occupancy prediction). This approach achieves leading multi-task perception performance on the nuScenes dataset. Additionally, we introduce a model-merging-based pre-training strategy, which further enhances multi-task accuracy. To tackle the third challenge, we build upon the HENet++ multi-task perception model and further refine it into an end-to-end autonomous driving model. This model can predict future movements of objects in the scene and generate future trajectory plans for the ego vehicle. Moreover, our framework supports multi-modal input from millimeter-wave radar and multiple cameras, achieving a lower collision rate on the nuScenes dataset than existing methods.

The contributions of this work can be summarized as follows:

- 1) We propose HENet, which is based on multi-view camera inputs and dense BEV features. Through the Hybrid Encoding, a U-shaped temporal BEV fusion module, and independent BEV encoding, it simultaneously predicts 3D object detection and BEV semantic segmentation.
- 2) Building upon the HENet model, we introduce the HENet++ perception framework. By simultaneously hybrid encoding for sparse foreground features and dense background voxel features, the framework enables end-to-end prediction for 3D object detection,

BEV semantic segmentation, and occupancy semantic segmentation, providing suitable features for each task. In addition, we introduce a model-merging-based pre-training strategy that further enhances multi-task accuracy. HENet++ achieves state-of-the-art end-to-end multi-task perception performance on the nuScenes dataset.

- 3) Based on the HENet++ perception framework, we further design an end-to-end autonomous driving model. Leveraging the extracted sparse foreground features and dense background features, HENet++ employs an attention-based world-prediction module to simultaneously perform prediction and ego-vehicle trajectory planning. HENet++ is the first work that leverages Radar and Camera for end-to-end autonomous driving. On the nuScenes dataset, the HENet++ model achieves a lower collision rate compared to existing methods.

2 Related work

2.1 Multi-View 3D Object Detection

3D object detection is a classic 3D perception task, aiming to predict the 3D bounding boxes of objects and determine the category and confidence of each predicted object. Early methods primarily predict objects from monocular images [4–11]. In recent years, multi-view cameras have become standard sensors on autonomous vehicles, offering richer perceptual information. Current multi-view 3D object detection approaches can be broadly categorized into two types based on view transformation strategies: BEV-based methods [12–23] and sparse query-based methods [24–33].

BEV-based Methods. BEVDet [12] employs the Lift-Splat-Shoot (LSS) [34] method to construct BEV features from multi-view image features using depth prediction. To mitigate inaccurate depth estimation in BEVDet, BEVDepth [13] incorporates camera parameters into the depth prediction network and enriches depth supervision with LiDAR point clouds. BEVDet4D [14] integrates temporal information by aligning BEV features across consecutive frames via ego-motion transformation. Building upon BEVDepth, BEVStereo [15] and STS [22] introduce temporal stereo techniques to refine depth estimation

accuracy. For long-term temporal modeling, BEVFormer [20] and Polarformer [19] treat BEV features as queries and apply cross-attention to aggregate historical frame information. BEVFormerV2 [21] further enhances BEVFormer by incorporating perspective view supervision. SOLO-Fusion [16] proposes a hierarchical fusion strategy that first combines short-term BEV features before integrating long-term sequences. HoP [23] designs a plug-and-play historical object prediction module compatible with various temporal 3D detectors. AeDet [17] introduces azimuth-equivariant convolutions and anchor designs to achieve consistent BEV representations across different orientations.

Sparse Query-based Methods. DETR3D [25] first extends DETR [35] by utilizing sparse 3D object query to index features. PETR [26] enhances DETR3D by aggregating image features with 3D position information, and PETRv2 [27] further introduces temporal information into 3D position embedding to allow temporal alignment for object positions. 3D-MAN [28] designs an alignment and aggregation module to extract temporal features from the memory bank that stores information generated by a single frame detector. Sparse4D [29] assigns and projects 4D keypoints to generate different views, scales, and timestamps. Sparse4Dv2 [30] improves the temporal fusion module to reduce the computational complexity and enable long-term fusion. StreamPetr [31] presents an efficient intermediate representation to transfer temporal information, like BEV-based methods, to avoid repeated calculation of features. Far3D [33] uses a perspective-aware aggregation module to capture features of long-range objects and designs a denoising method to improve query propagation. SparseBEV [32] designs a scale-adaptive self-attention module for query feature interaction and proposes spatio-temporal sampling and adaptive mixing to aggregate temporal features into current queries.

3D object detection primarily focuses on foreground objects, and Sparse Query-based Methods hold distinct advantages over BEV-based approaches. This advantage may stem from the inherently sparse nature of object detection outcomes. Even when dense features are extracted, the process still requires subsequent extraction of sparse object features from them. Additional

processing steps—such as depth estimation, projection, and heatmap clustering—introduce more cumulative errors. Therefore, Sparse Query-based Methods, which directly extract object features, tend to achieve superior performance.

2.2 BEV Semantic Segmentation

As the name suggests, BEV Semantic Segmentation aims to predict a dense map from a bird’s-eye view perspective, where each grid cell is assigned a semantic label. Numerous studies [34, 36–39] follow a paradigm similar to BEVDet [12], differing in their task-specific heads. VPN [39] trains its model in synthetic 3D environments and applies domain adaptation for real-world deployment. M2BEV [40] effectively transforms multi-view 2D image features into 3D BEV representations within ego-vehicle coordinates, enabling a unified encoder for multiple tasks. CVT [41] leverages cross-view attention to implicitly learn perspective-to-BEV mappings, incorporating camera-specific positional embeddings based on calibration parameters. HDMapNet [42] encodes multi-view image features to predict vectorized map elements directly in BEV space.

Unlike 3D object detection, BEV semantic segmentation mainly focuses on background map elements. Its final step involves decoding categories from BEV features, and therefore, the core methodology of BEV semantic segmentation predominantly utilizes BEV feature maps as its 3D representation.

2.3 Occupancy Prediction

Occupancy perception aims to divide space into 3D grids and predict whether each grid is occupied by any object. It was initially proposed to represent irregularly shaped objects, while subsequent works have further extended this by assigning semantic labels to each occupied grid. MonoScene [43] represents a pioneering approach relying solely on RGB inputs. TPVFormer [44] integrates multi-view camera inputs and employs transformer-based architecture to project features into tri-perspective view representation. SurroundOcc [45] extends high-dimensional BEV features into occupancy representations through direct spatial cross-attention for geometric modeling. VoxFormer [46] proposes a two-stage transformer framework for semantic

scene completion, generating complete 3D volumetric semantics from 2D images. FlashOcc [47] transforms channels into height dimensions, efficiently lifting BEV representations to 3D space with significantly improved computational performance. FBOcc [48] introduces a front-to-back view transformation module to overcome limitations of conventional view transformations. UniOcc [49] and RenderOcc [50] utilize NeRF [51] for direct 3D semantic occupancy prediction, though rendering speed constrains their practical efficiency. FastOcc [52] enhances the occupancy prediction head to achieve accelerated inference. COTR [53] constructs compact 3D occupancy representations through explicit-implicit view transformation and coarse-to-fine semantic grouping.

Occupancy prediction focuses on both foreground and background elements in a scene, and captures more content than BEV semantic segmentation. By nature, occupancy is essentially a dense 3D semantic segmentation task. Therefore, similar to how object detection favors sparse features, occupancy prediction tends to perform better with dense representations such as BEV or voxel features.

2.4 End-to-end Multi-task Learning

End-to-end multi-task learning aims to solve multiple tasks, including those mentioned above, within a single model. It eliminates redundant computations and holds significant practical value. A limited number of studies have explored multi-task perception, including 3D object detection and BEV segmentation [38, 39, 54, 55]. Current works often follow the joint training strategy of BEVFormer [20], which generates a unified BEV feature map for detection and segmentation. PETRv2 [27] initializes two query sets for detection and segmentation tasks and sends each query set to the corresponding task heads. These works show conflicts arising when combining 3D object detection and BEV segmentation.

ST-P3 [56] first integrates perception, prediction, and planning into an end-to-end framework. This category of tasks, which takes sensor information as input and directly outputs the ego vehicle’s planned trajectory or control signals, is referred to as end-to-end autonomous driving. UniAD [57] adopts a feature extraction approach

similar to BEVFormer [20], with relatively complex feature or result passing among task-specific decoders. VAD [58] achieves trajectory planning by representing the driving scene in a fully vectorized manner. PARA-Drive [1] first explored the use of LiDAR and cameras for end-to-end autonomous driving and noted that overly complex connections among multiple tasks should be avoided to prevent cumulative errors. GenAD [2] first extracts BEV features, then extracts sparse detection and sparse mapping features from them, and further performs planning. SparseDrive [3] directly extracts sparse detection and sparse mapping features from image features, thereby reducing cumulative errors and improving prediction performance. MomAD [59] proposed a momentum-aware planning approach to enhance prediction and planning outcomes. BridgeAD [60] leverages historical prediction and planning trajectories to improve planning results. DiffusionDrive [61] designed a truncated diffusion model to generate diverse candidate trajectories. The works mentioned above propose various multi-task paradigms. Compared to dense features, purely sparse 3D features only focus on foreground categories such as vehicles and lane lines, resulting in insufficiently comprehensive information. However, approaches entirely based on dense features still require extracting object instances from them. As analyzed in Section 2.1, their prediction accuracy is inferior to directly extracting sparse features. Our proposed method not only extracts dense features of the entire scene, constrained by the occupancy task, but also extracts sparse features of foreground objects, constrained by 3D object detection, thereby leveraging more comprehensive information for prediction and planning. Meanwhile, HENet++ is the first framework that leverages Radar and Camera for end-to-end autonomous driving.

3 HENet: Hybrid Encoding and Multi-task Perception for BEV Paradigm

As shown in Figure 2, the HENet framework comprises three stages. Given temporal multi-view image inputs, a hybrid image encoding network uses image encoders of varying complexity to extract long-sequence BEV features and short-term BEV features. We then leverage a temporal

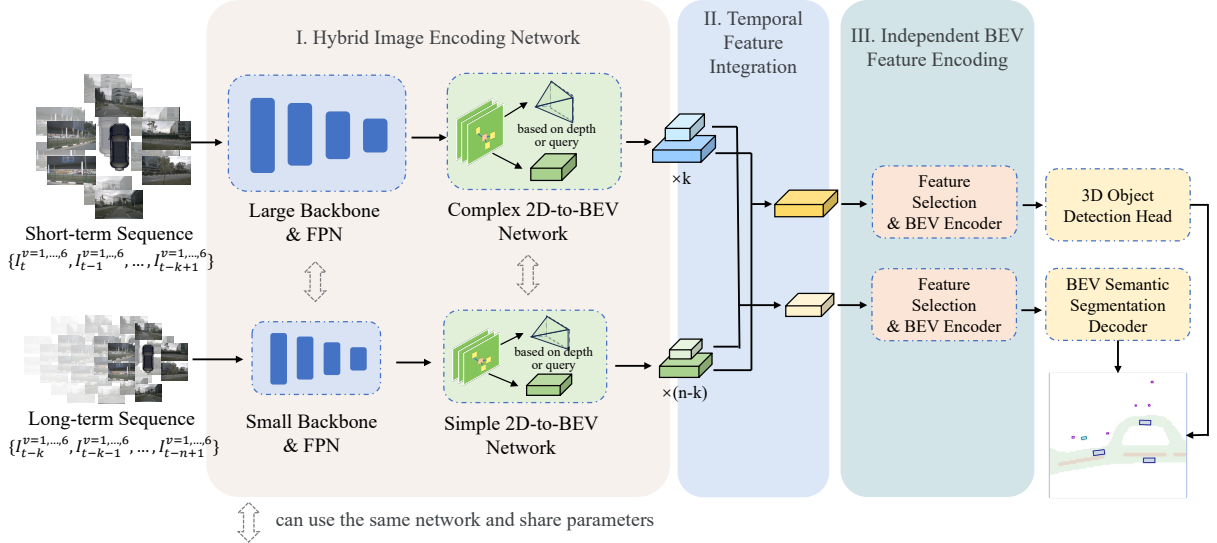


Fig. 2: Overall architecture of HENet. I) Hybrid Image Encoding Network uses image encoders of varying complexity to encode long-sequence frames and short-term images, respectively. II) Temporal Feature Integration module fuses multi-frame features from the various encoders. III) Independent BEV Feature Encoding prepares separate BEV feature maps for different tasks.

feature integration module, incorporating an attention mechanism, to aggregate the multi-frame BEV features. Subsequently, the BEV features at different grid resolutions are distributed to dedicated encoders and decoders for each specific task, ultimately yielding the multi-task perception results.

3.1 Hybrid Image Encoding Network

As shown in Fig. 2, the hybrid image encoding network employs two image encoders of distinct complexities to process different temporal inputs. The first encoder handles high-resolution short-term frames, passing them through a large image backbone (*e.g.*, VoVNetV2-99 [62]) and a feature pyramid network (FPN) [63], and subsequently applies a complex 2D-to-BEV network to generate high-precision BEV features. Specifically, we choose BEVStereo [15] as the complex 2D-to-BEV network. The second encoder processes long-term sequences by down-sampling the inputs to low resolution, using a lightweight backbone (*e.g.*, ResNet-50 [64]) with FPN for efficient feature extraction, followed by a simplified 2D-to-BEV module. Specifically, we choose BEVDepth [13] as the lightweight 2D-to-BEV network. Both pathways employ BEVPoolv2 [65] to project frustum

Algorithm 1 Pseudo-code for Section 3.2

Input: A series of BEV features $\{f_{-n+1}, \dots, f_{-1}, f_0\}$. f_0 represents BEV feature of the current frame and f_{-i} corresponds to the i^{th} frame before f_0 .

```

for  $i$  from 0 to  $n-2$  do
     $f_{-(i+1)} \leftarrow \text{AFFM}(f_{-i}, f_{-(i+1)})$ 
end for
for  $i$  from  $n-2$  to 0 do
     $f_{-i} \leftarrow \text{AFFM}(f_{-(i+1)}, f_{-i})$ 
end for
return  $f_0$ 

```

features into multi-scale BEV representations. Based on our experimental analysis, we use BEV feature maps with resolutions of 256×256 and 128×128 for 3D object detection and BEV semantic segmentation, respectively. Some parts of the hybrid image encoders can be shared. For example, we can use a single backbone (*e.g.*, a single ResNet-50) with different 2D-to-BEV networks.

3.2 Temporal Feature Integration

Following the extraction of multi-frame BEV features by the hybrid image encoding network, we fuse them using a temporal integration module, as illustrated in Fig. 3. This module operates through complementary backward and forward processes. The backward process propagates features from the current frame to past frames, whereas the forward

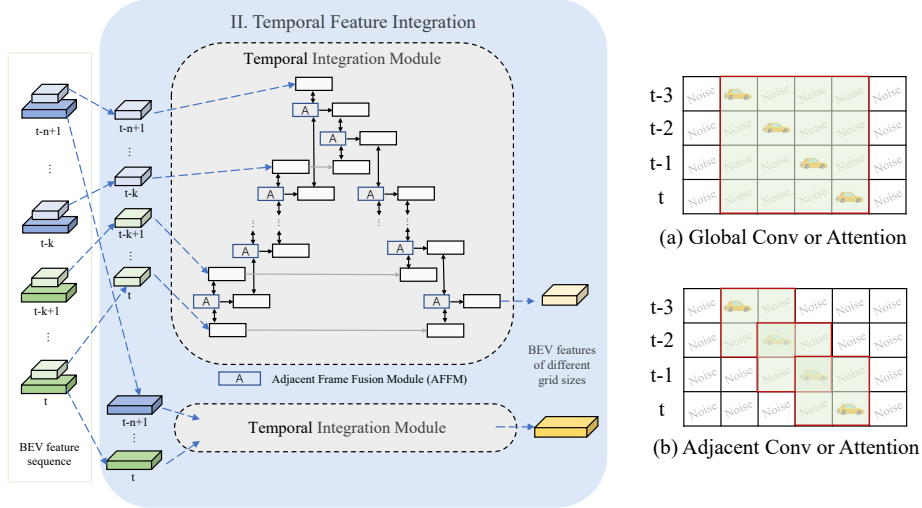


Fig. 3: Architecture of Temporal Feature Integration module. We propose the adjacent frame fusion module (AFFM) and adopt the temporal fusion strategy with temporal backward and forward processes.

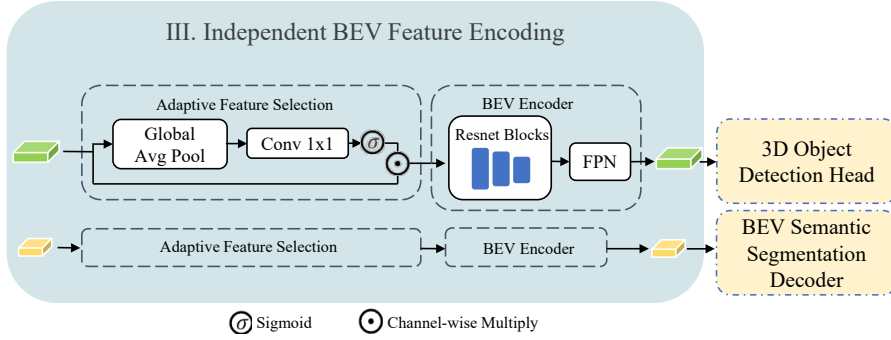


Fig. 4: Design of Independent BEV Feature Encoding. Each task decoder is provided with BEV feature maps in different grid sizes through independent adaptive feature selection and BEV encoding.

process aggregates features from past frames to the current one. Each step in these processes employs a weight-sharing Adjacent Frame Fusion Module (AFFM) that uses a cross-attention mechanism to fuse BEV features from two adjacent frames. The pseudo-code for this entire procedure is provided in Algorithm 1. Specifically, given BEV features from two frames, f_i and f_j , the AFFM operation can be formulated as:

$$\text{AFFM}(f_i, f_j) = f_j + \gamma \times \text{Avg}(\text{Atn}(\langle f_i, f_j \rangle, f_i, f_i), \text{Atn}(\langle f_i, f_j \rangle, f_j, f_j)), \quad (1)$$

where $\text{Avg}(\cdot)$ represents average operator, γ is a learnable scaling parameter, $\langle \cdot, \cdot \rangle$ denotes concatenation, and $\text{Atn}(\cdot, \cdot, \cdot)$ is a cross attention module:

$$\text{Atn}(q, k, v) = \text{softmax}\left(\frac{qk^\top}{\sqrt{d}}\right)v. \quad (2)$$

In the backward process, $j = i - 1$, while in the forward process, $j = i + 1$.

As shown in Fig. 3, adjacent attention reduces noise compared to global attention or cross-frame

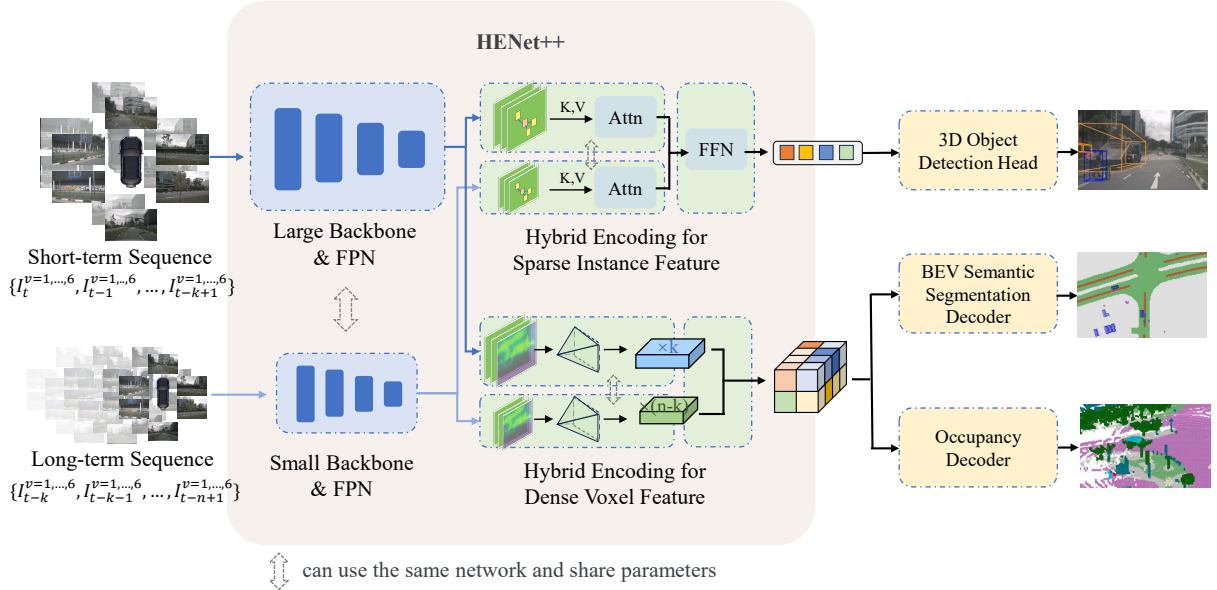


Fig. 5: Overall architecture of HENet++. By simultaneously hybrid encoding for sparse foreground features and dense background voxel features, the framework enables end-to-end multi-task prediction. In addition, we introduce a model-merging-based pre-training strategy that further enhances multi-task performance.

convolutions. This enables the AFFM to align moving objects and suppress redundant background information.

3.3 Independent BEV Feature Encoding

To mitigate conflicts between tasks, HENet proposes a preliminary solution that provides separate BEV feature maps for different tasks. Based on our empirical analysis in [66], different tasks prefer different sizes of BEV features. Thus, after obtaining the fused multi-scale BEV features, we first assign different-sized BEV features to other tasks. We then independently encode the BEV features for each task. Inspired by BEVFusion [67], the proposed encoding process comprises adaptive feature selection and BEV encoding. Specifically, the adaptive feature selection $f_{adaptive}(\cdot)$ applies a channel attention module to select important features:

$$f_{adaptive}(\mathbf{F}) = \sigma(\mathbf{W}f_{avg}(\mathbf{F})) \cdot \mathbf{F}, \quad (3)$$

where $\mathbf{F} \in \mathbb{R}^{X \times Y \times C}$ is the BEV features, \mathbf{W} denotes linear transform matrix, f_{avg} indicates the global average pooling, and σ represents the Sigmoid function. For the BEV encoder, we adopt

three ResNet [64] residual blocks and a simple FPN [63] to perform local feature integration on the BEV feature map. Notably, the adaptive feature selection and BEV encoders for different tasks employ the same architecture but maintain independent weights.

3.4 Decoders and Losses

Our model employs CenterPoint [68] as the 3D object detection decoder, with its classification and regression losses denoted as \mathcal{L}_{cls} and \mathcal{L}_{bbox} , respectively. For BEV semantic segmentation, we use a SegNet-based decoder [69] optimized with focal loss \mathcal{L}_{seg} . Additionally, a binary cross-entropy loss \mathcal{L}_{depth} is applied for depth estimation. The total loss is a weighted sum:

$$\mathcal{L} = \alpha_{depth}\mathcal{L}_{depth} + \alpha_{cls}\mathcal{L}_{cls} + \alpha_{bbox}\mathcal{L}_{bbox} + \alpha_{seg}\mathcal{L}_{seg} \quad (4)$$

, where α is a balancing weight.

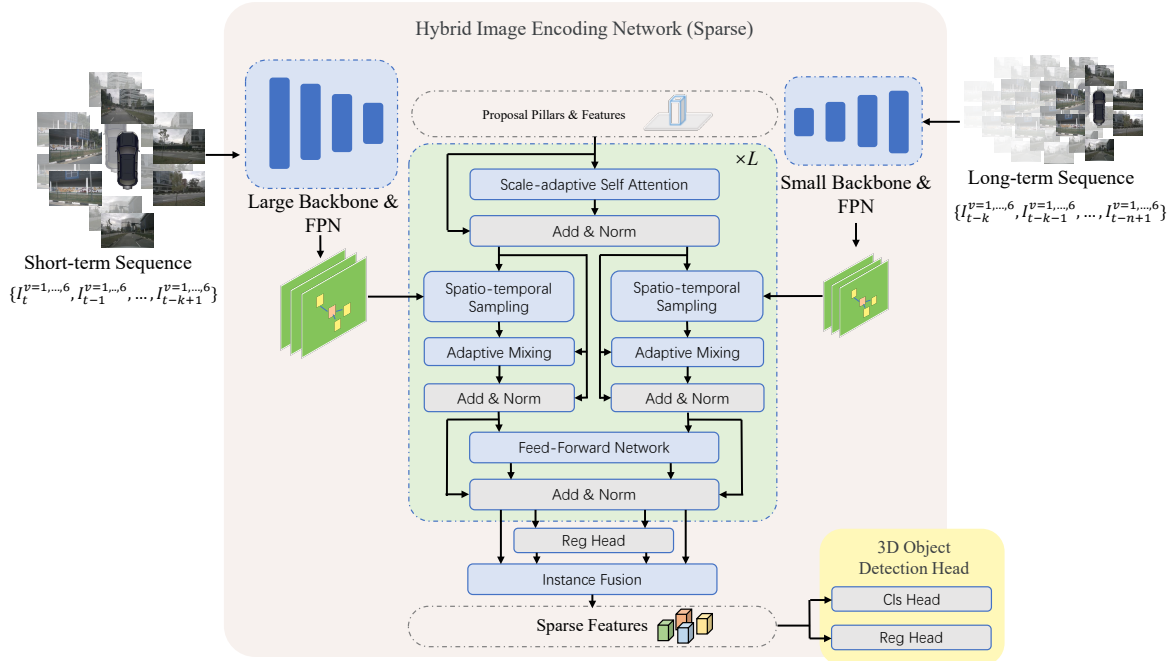


Fig. 6: Design of Hybrid Image Encoding Network for sparse feature extraction.

4 HENet++: Hybrid Encoding and Multi-task Perception for A Dense-Sparse Collaborative Framework

4.1 Overall framework: Joint Sparse and Dense Encoding

Based on further analysis of the characteristics of different tasks in existing work, we have identified potential underlying causes of multi-task conflicts. The output of tasks such as 3D object detection is inherently sparse. Even if dense features are extracted, sparse object features must still be distilled from the dense features. Additional steps, such as depth estimation, projection, and heatmap clustering, introduce more cumulative errors. Consequently, sparse tasks favor sparse query-based architectures that directly extract instance features. Similarly, tasks such as BEV semantic segmentation and occupancy prediction produce dense outputs, making them more compatible with BEV or Voxel-based architectures.

To enhance multi-task accuracy and obtain more comprehensive foreground and background information, we propose the HENet++ framework,

building upon the HENet framework. As shown in Figure 5, HENet++ innovatively introduces the simultaneous extraction of sparse foreground features and dense panoramic features. To achieve this, we extend hybrid encoding to be compatible with both sparse and dense feature extraction. Furthermore, by employing a pre-training strategy based on multi-task model consolidation, we can further improve multi-task performance.

4.2 Hybrid Encoding for Sparse Instance Feature

As shown in Figure 5, Hybrid Encoding employs two backbones and FPNs to extract 2D feature maps from short-term high-resolution images and long-term low-resolution images, further deriving sparse instance features and dense voxel features from them. The method for extracting voxel features is identical to the approach described in Section 3.1 and Section 3.2, which involves two 2D-to-BEV networks and a U-shaped Temporal Feature Integration module.

Regarding the method for extracting sparse features, we have made modifications based on SparseBEV [32]. Similarly, we adopt learnable initialization and Scale-adaptive Self-Attention to

initialize queries $q \in \mathbb{R}^{N \times d}$:

$$q = \text{LayerNorm}(Q + \text{Softmax}(\frac{QK^T}{\sqrt{d}} - \tau D)V), \quad (5)$$

where $Q, K, V \in \mathbb{R}^{N \times d}$ is the query itself, N refers to the number of queries, d is the channel dimension, and τ is a scalar to control the receptive field for each query. These queries are simultaneously used to query both short-term and long-term features.

Supposing there are k frames for the short-term image features f_{short} , $n - k$ frames for the long-term encoder f_{long} , and S sampling points per frame, Two separate Spatio-temporal Sampling [32] respectively extract two sets of sampling features $P_{short} \in \mathbb{R}^{k \times S \times C}$ and $P_{long} \in \mathbb{R}^{(n-k) \times S \times C}$ from the image features. Next, obtain the short-term instance feature $q'_{short} \in \mathbb{R}^{N \times d}$ and the long-term instance feature $q'_{long} \in \mathbb{R}^{N \times d}$ through Adaptive Mixing:

$$\langle q_{short}, q_{long} \rangle = \text{ReLU}(\text{LayerNorm}(\langle P_{short}, P_{long} \rangle \cdot \text{Linear}^{C \times C}(\langle q, q \rangle))), \quad (6)$$

$$q'_{short} = \text{ReLU}(\text{LayerNorm}(q_{short}^T \cdot \text{Linear}^{kS \times kS}(q))), \quad (7)$$

$$q'_{long} = \text{ReLU}(\text{LayerNorm}(q_{long}^T \cdot \text{Linear}^{(n-k)S \times (n-k)S}(q))), \quad (8)$$

where the network weights for Channel Mixing (Equation 6) are shared between long-term and short-term features, while Point Mixing (Equation 7 and 8) employs two separate networks for long-term and short-term features, respectively. q'_{short} and q'_{long} are fed into an FFN before proceeding to the next iteration of Self-Attention, Sampling, and Mixing, repeating this process until L iterations are completed.

After L iterations, N short-term instance features and N long-term instance features are extracted. Although they were initially one-to-one corresponding in the original queries q , the regions each query attends to continuously shift during the attention process, potentially resulting in different instances being matched. Additionally, there may be overlaps between these two sets of features. Therefore, directly merging them into N features or simply concatenating them into $2N$ features is

unreasonable. Here, we employ the regression head from the 3D object detection head, using this MLP to decode the bounding boxes of instances, and perform deduplication, similar to non-maximum suppression, to identify multiple features corresponding to the same instance. For each instance, the associated C -dimensional feature vectors are fused into a single vector via channel-wise max pooling.

4.3 Pretrain based on Model Merging

In the training process of a multi-task model, how to initialize the parameters is also very important. During our experiments, we found that using the encoder parameters from a model pre-trained on a single 3D task and loading the corresponding decoder parameters leads to faster convergence and higher accuracy compared to loading backbone and neck parameters pre-trained on 2D tasks. However, since the multi-task model shares the same encoder, determining which single-task model should be used to provide the pre-trained weights for the encoder is a question worth investigating. Experiments show that when using a 3D object detection model to initialize the encoder, the resulting multi-task model achieves higher accuracy in 3D object detection, while the accuracy of other tasks decreases. Similarly, when using a single-task occupancy model for pre-training, the occupancy accuracy is higher, but the accuracy of other tasks is reduced.

Algorithm 2 Model Merge for Pretrain, Modified from [70]

Input: Single-task encoder $f_{1..K}$, Number of linear layers J , inner product matrices $G_i^{(j)} = X_i^{(j)T} X_i^{(j)}$ for all linear layers $1 \leq j \leq J$ and single-task encoder $1 \leq i \leq K$, Scaling factor of non-diagonal items α

for j **in** $1, 2, \dots, J$ **do**
 $W_1^{(j)}, W_2^{(j)}, \dots, W_K^{(j)} \leftarrow \text{getWeights}(f_{1..K}, j)$
Reduce non-diagonal items of inner product matrices $G_i^{(j)}$ as $\tilde{G}_i^{(j)} \leftarrow \alpha G_i^{(j)} + (1 - \alpha) \text{diag}(G_i^{(j)})$
 $W_M^{(j)} \leftarrow (\sum_{i \in \mathcal{K}} \tilde{G}_i^{(j)})^{-1} \sum_{i \in \mathcal{K}} (\tilde{G}_i^{(j)} W_i^{(j)})$ and set the weight as $W_M^{(j)}$ in f_M
end for
Average weights as $W_M = \frac{1}{K} \sum_{i \in \mathcal{K}} W_i$ for weights other than linear weights in f_M

Model merging, which used in natural language processing, combines multiple single-task models

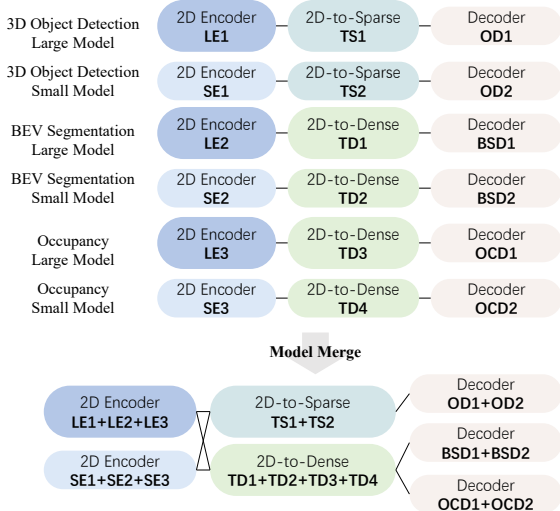


Fig. 7: The merging process of the HENet++ pre-trained models.

into one for direct multi-task inference. We also attempted to apply model merging methods like Regmean [70] directly to 3D vision multi-task learning, but it performed poorly. This is likely due to the complex architectures and task representations in 3D vision models. However, inspired by this approach, we consolidated the encoder weights from multiple single-task models into a single encoder and used it as a pre-trained initialization, which achieved promising results.

The model merging method is outlined in Algorithm 2. Specifically, for the weight matrices in convolutional networks and linear layers, we apply Regression Mean. For other learnable parameters, we directly compute their average. The architectural design of HENet++ involves three tasks. Each task processes both short-term and long-term components, which are inherited from two differently sized models, respectively. The process of merging these models to serve as multi-task pre-training is illustrated in Figure 7.

4.4 Decoders and Losses

Our model employs two separate MLPs to predict object categories and bounding boxes from the sparse features. The classification loss is Focal Loss, denoted as \mathcal{L}_{cls} , and the bounding box loss is L1 Loss, denoted as \mathcal{L}_{bbox} . For BEV semantic segmentation, we use a SegNet-based decoder [69] optimized with focal loss \mathcal{L}_{seg} . For Occupancy, we

use a simple MLP as decoder with focal loss \mathcal{L}_{occ} . Additionally, a binary cross-entropy loss \mathcal{L}_{depth} is applied for depth estimation. The total loss is a weighted sum:

$$\mathcal{L} = \alpha_{depth}\mathcal{L}_{depth} + \alpha_{cls}\mathcal{L}_{cls} + \alpha_{bbox}\mathcal{L}_{bbox} + \alpha_{seg}\mathcal{L}_{seg} + \alpha_{occ}\mathcal{L}_{occ} \quad (9)$$

, where α is a balancing weight.

5 End-to-End Autonomous Driving Based on HENet++

As shown in Figure 8, we extend the HENet++ framework to address end-to-end autonomous driving. We design a simple yet effective iterative prediction and planning decoder. Compared to existing methods that rely solely on a single form of 3D features, HENet++ can leverage more comprehensive information for planning. Sparse instance features provide learnable queries for object motion prediction, serving as the foundation for both prediction and planning, while dense panoramic features offer more complete scene information.

Specifically, the prediction and planning decoder of HENet++ employs N Transformer layers for iterative prediction. Before the iteration begins, the top- K 3D object detection results with the highest confidence scores, along with their instance features F_{det} , are first taken. The positional encodings of their bounding box centroids are concatenated to form K vectors $F_{1,2,\dots,K}$. The historical trajectory of the ego vehicle, navigation waypoints, acceleration, velocity, and other information are passed through a linear layer to project them into higher dimensions, and the positional encoding of the origin is concatenated to obtain the ego vehicle vector F_0 . The occupancy grid network and voxel features are downsampled, and then the semantic category and features of each grid are concatenated in the channel dimension with the positional encoding of the grid coordinates to obtain the occupancy grid tokens F_{occ} . The initial query is defined as $Q_0 = \langle F_0, F_{1,2,\dots,K} \rangle$. In the i -th iteration, Q_{i-1} is used as the initial query. It then undergoes self-attention on Q_{i-1} , cross-attention with Q_0 as key-value, cross-attention with F_{occ} as key-value, and a feed-forward network to produce Q_i . Meanwhile, the output of each

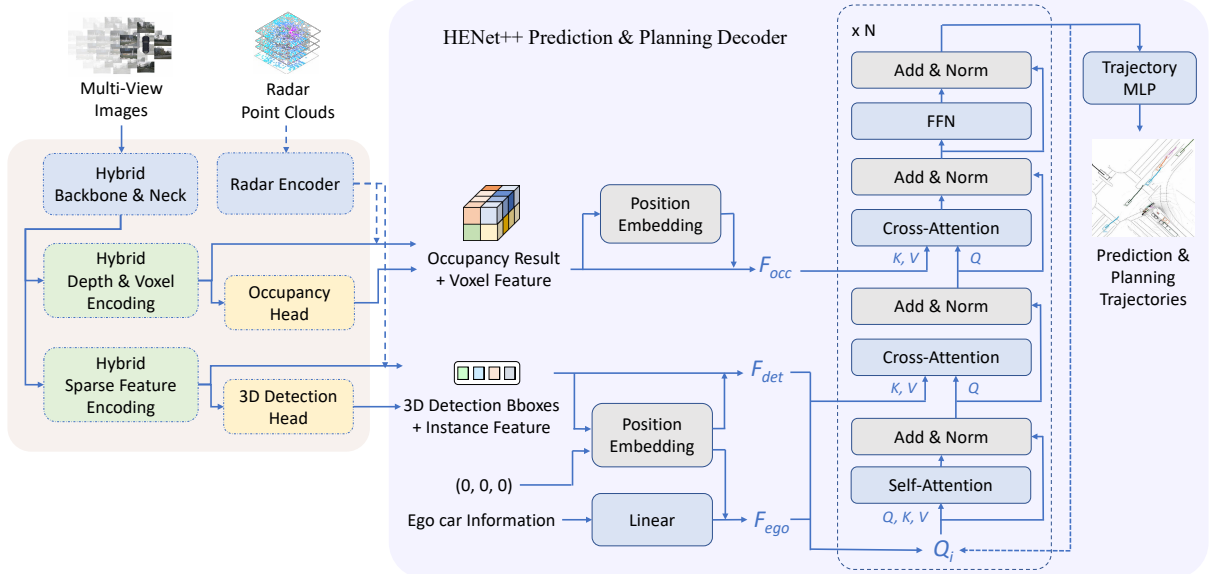


Fig. 8: Architecture of the HENet++ End-to-end Autonomous Driving framework. We design an attention-based trajectory planner that utilizes instance features (including the ego vehicle’s features) as queries, and instance features combined with panoramic dense features as key-value pairs, enabling simultaneous iterative prediction of future states and ego planning. The compatibility of HENet++ with both dense and sparse features also facilitates straightforward extension to multi-modal inputs.

layer is decoded by a trajectory MLP to obtain the trajectory $Tra_{j_0,1,\dots,K}$ of each object. Tra_{j_0} represents the planned trajectory of the ego vehicle, while $Tra_{j_1,\dots,K}$ represent the predictions for the corresponding objects.

The HENet++ framework is compatible with both sparse and dense features, enabling relatively straightforward integration with existing multi-modal feature fusion methods. For example, by utilizing the Radar encoder from RCBEVDet++ [71] along with the interpolation method described in the paper, both sparse and dense Radar features can be obtained. The CAMF module in [71] can be further employed to integrate Radar features into the end-to-end model.

Denoting the perception Loss in Section 4.4 as \mathcal{L}_{prec} , the end-to-end model introduces three additional losses. The first is the L1 loss between the ego vehicle’s future trajectory and the ground truth, denoted as \mathcal{L}_{plan} . The second is the L1 loss between the future trajectories of other objects and their ground truth, denoted as \mathcal{L}_{pred} . Each trajectory Tra_{j_i} consists of t future coordinate points in the horizontal Cartesian coordinate system: $\{(x_{i1}, y_{i1}), (x_{i2}, y_{i2}), \dots, (x_{it}, y_{it})\}$. The third

is a collision constraint \mathcal{L}_{col} , defined as follows:

$$D(Tra_{j_a}, Tra_{j_b}, t_i) = \sqrt{(x_{at_i} - x_{bt_i})^2 + (y_{at_i} - y_{bt_i})^2}, \quad (10)$$

$$P(Tra_{j_a}, Tra_{j_b}, t_i) = \begin{cases} 3 - D(Tra_{j_a}, Tra_{j_b}, t_i), \\ \quad \text{if } D(Tra_{j_a}, Tra_{j_b}, t_i) < 3 \\ 0, \quad \text{else} \end{cases}, \quad (11)$$

$$\mathcal{L}_{col} = \sum_{i=1}^K \sum_{j=1}^t P(Tra_{j_0}, Tra_{j_i}, t_j). \quad (12)$$

The total loss is a weighted sum:

$$\mathcal{L} = \mathcal{L}_{prec} + \alpha_{plan} \mathcal{L}_{plan} + \alpha_{pred} \mathcal{L}_{pred} + \alpha_{col} \mathcal{L}_{col} \quad (13)$$

, where α is a balancing weight.

6 Experiments

6.1 Implementation Details

We train HENet in end-to-end manner for multi-tasks, including 3D object detection and BEV

Table 1: Comparison of end-to-end multi-task learning on the nuScenes val set. Time/E represent the training time per epoch with FP32 on $8 \times A800$ GPUs. $mIoU_v$, $mIoU_a$, and $mIoU_d$ represent the mIoU for vehicles, drivable area, and lane & road divider, respectively.

Methods	Backbone	Frames	Time/E	Detection		BEV Segmentation				Occupancy	
				NDS \uparrow	mAP \uparrow	mIoU \uparrow	IoU \uparrow	mIoU \uparrow	mIoU \uparrow	IoU \uparrow	mIoU \uparrow
VPN [39]	ResNet50	1	-	33.4	25.7	43.8	37.3	76.0	18.0	-	-
LSS [34]	ResNet50	1	-	41.0	34.4	45.0	42.8	73.9	18.3	-	11.4
BEVFormer-S [20]	ResNet101	1	-	45.3	38.0	47.3	44.4	77.6	19.8	-	-
BEVFormer [20]	ResNet101	5	213min	52.0	41.2	49.4	46.7	77.5	23.9	-	30.5
OccNet [72]	ResNet101	5	230min	52.0	41.2	24.6	12.9	47.2	13.8	41.1	27.0
UniAD [57]	ResNet101	6	253min	49.9	38.2	-	-	69.1	25.7	62.3	-
PARA-Drive [1]	ResNet101	6	240min	48.0	37.0	-	-	71.0	33.0	63.6	-
HENet	R101 & R50	2 + 3	60min	56.4	47.1	53.9	44.5	77.0	40.1	-	-
HENet++	R101 & R50	2 + 3	82min	60.5	53.0	55.4	45.8	79.3	41.1	68.2	46.4
PETrv2 [27]	V2-99	2	75min	49.5	40.1	57.6	49.4	79.1	44.3	-	-
HENet	V2-99 & R50	2	58min	58.0	48.7	56.9	47.6	80.2	42.8	-	-
HENet	V2-99 & R50	2 + 7	71min	59.9	49.9	58.0	49.5	81.3	43.4	-	-
HENet++	V2-99 & R50	5 + 11	205min	63.7	56.7	58.3	49.6	81.8	43.7	70.8	47.3

Table 2: Comparison of End-to-end Autonomous Driving results on nuScenes val set. L2 refers to the L2 error between the predicted trajectory and the ground-truth trajectory of human driving.

Method	Input	Backbone	UniAD Metrics								VAD/STP3 Metrics							
			L2 (m) \downarrow				Collision Rate (%) \downarrow				L2 (m) \downarrow				Collision Rate (%) \downarrow			
			1s	2s	3s	Avg.	1s	2s	3s	Avg.	1s	2s	3s	Avg.	1s	2s	3s	Avg.
ST-P3 [56]	C	EfficientNet-b4	1.72	3.26	4.86	3.28	0.44	1.08	3.01	1.51	1.33	2.11	2.90	2.11	0.23	0.62	1.27	0.71
OccNet [72]	C	ResNet101-DCN	1.29	2.13	2.99	2.14	0.21	0.59	1.37	0.72	-	-	-	-	-	-	-	-
UniAD [57]	C	ResNet101	0.48	0.96	1.65	1.03	0.05	0.17	0.71	0.31	0.45	0.70	1.04	0.73	0.62	0.58	0.63	0.61
VAD-Tiny [58]	C	ResNet50	0.60	1.23	2.06	1.30	0.31	0.53	1.33	0.72	0.46	0.76	1.12	0.78	0.21	0.35	0.58	0.38
VAD-Base [58]	C	ResNet101	0.54	1.15	1.98	1.22	0.04	0.39	1.17	0.53	0.41	0.70	1.05	0.72	0.07	0.17	0.41	0.22
PARA-Drive [1]	C	ResNet50	-	-	-	-	-	-	-	-	0.25	0.46	0.74	0.48	0.14	0.23	0.39	0.25
GenAD [2]	C	ResNet50	0.36	0.83	1.56	0.91	0.06	0.23	1.00	0.43	0.28	0.49	0.78	0.52	0.08	0.14	0.34	0.19
SparseDrive [3]	C	ResNet50	0.44	0.92	1.69	1.01	0.07	0.19	0.71	0.32	0.29	0.58	0.96	0.61	0.01	0.05	0.18	0.08
MomAD [59]	C	ResNet50	0.43	0.88	1.62	0.98	0.06	0.16	0.68	0.30	0.31	0.57	0.91	0.60	0.01	0.05	0.22	0.09
SSR [73]	C	ResNet50	0.24	0.65	1.36	0.75	0.00	0.10	0.36	0.15	0.18	0.36	0.63	0.39	0.01	0.04	0.12	0.06
BridgeAD-S [60]	C	ResNet50	-	-	-	-	-	-	-	-	0.29	0.57	0.92	0.59	0.01	0.05	0.22	0.09
BridgeAD-B [60]	C	ResNet101	-	-	-	-	-	-	-	-	0.28	0.55	0.92	0.58	0.00	0.04	0.20	0.08
DiffusionDrive [61]	C	ResNet50	-	-	-	-	-	-	-	-	0.27	0.54	0.90	0.57	0.03	0.05	0.16	0.08
HENet++	C	ResNet50	0.41	1.27	2.63	1.44	0.02	0.10	0.39	0.17	0.25	0.56	1.02	0.61	0.01	0.05	0.12	0.06
HENet++	RC	ResNet50	0.39	1.11	2.36	1.29	0.00	0.06	0.33	0.13	0.24	0.50	0.91	0.55	0.01	0.03	0.10	0.05

semantic segmentation in the same way as LSS [34]. We choose VovNet-99 [9, 62] with 640×1152 image resolution for the large image encoder and select ResNet-50 [64] with 256×704 image resolution for the small image encoder, respectively. For the input temporal sequence, we set short-term frame number $k = 2$ and long-term frame number $n = 9$. The weights of the hybrid image encoding network are initialized from pre-trained 3D detectors. As analyzed in [66], we choose BEV grid sizes of 0.4m (256×256 BEV size) and 0.8m (128×128 BEV size) for 3D object detection and BEV semantic segmentation, respectively. The end-to-end multi-task models are trained for 60 epochs without CBGS.

Besides, to further compare HENet with some single-task methods, we train the single 3D object detection models of HENet for 12 epochs with CBGS [75].

For HENet++ , we choose VovNet-99 [9, 62] with 640×1600 image resolution for the large image encoder and select ResNet-50 [64] with 256×704 image resolution for the small image encoder, following [32]. For the input temporal sequence, we set short-term frame number $k = 5$ and long-term frame number $n = 11$. For the Hybrid Encoding for sparse features, we set query number $N = 900$ and layer number $L = 6$. We also separately trained three single-task models with Hybrid Encoding,

Table 3: Comparison of 3D object detection results on the nuScenes val set. * indicates the result is benefited from the perspective pre-training. † indicates using one temporal frame information. ‡ denotes integrating two or more temporal frames. The best and second best results are marked in red and blue.

Methods	Backbone	NDS↑	mAP↑	mATE↓	mASE↓	mAOE↓	mAVE↓	mAAE↓
BEVDet [12]	ResNet50	37.9	29.8	0.725	0.279	0.589	0.860	0.245
BEVDet4D [14]†	ResNet50	45.7	32.2	0.703	0.278	0.495	0.354	0.206
PETrv2 [27]†	ResNet50	45.6	34.9	0.700	0.275	0.580	0.437	0.187
BEVStereo [15]†	ResNet50	50.0	37.2	0.598	0.270	0.438	0.367	0.190
SOLOFusion [16]‡	ResNet50	53.4	42.7	0.567	0.274	0.511	0.252	0.181
Sparse4Dv2 [30]‡	ResNet50	53.9	43.9	0.598	0.270	0.475	0.282	0.179
StreamPETR [31]‡	ResNet50	54.0	43.2	0.581	0.272	0.413	0.295	0.195
SparseBEV [32]‡	ResNet50	54.5	43.2	0.606	0.274	0.387	0.251	0.186
HENet ‡	ResNet50	55.4	43.7	0.512	0.262	0.367	0.285	0.213
PETR [26]*	ResNet101-DCN	44.1	36.6	0.717	0.267	0.412	0.834	0.190
BEVDepth [13]*†	ResNet101	53.5	41.2	0.565	0.266	0.358	0.331	0.190
BEVFormer [20]*‡	ResNet101-DCN	51.7	41.6	0.673	0.274	0.372	0.394	0.198
HoP-BEVFormer [23]*‡	ResNet101-DCN	55.8	45.4	0.565	0.265	0.327	0.337	0.194
StreamPETR [31]*‡	V2-99	57.1	48.2	0.569	0.262	0.315	0.257	0.199
SOLOFusion [16]*‡	ResNet101	58.2	48.3	0.503	0.264	0.381	0.246	0.207
SparseBEV [32]*‡	ResNet101	59.2	50.1	0.562	0.265	0.321	0.243	0.195
Far3D [33]*‡	ResNet101	59.4	51.0	0.551	0.258	0.372	0.238	0.195
HENet *‡	V2-99 & ResNet50	59.9	50.2	0.465	0.261	0.335	0.267	0.197
HENet++ *‡	V2-99 & ResNet50	65.1	57.3	0.506	0.252	0.182	0.225	0.195

Table 4: Comparison of 3D object detection results on nuScenes test set. The best and second best results are marked in red and blue. ‡uses test-time augmentation.

Methods	Backbone	NDS↑	mAP↑	mATE↓	mASE↓	mAOE↓	mAVE↓	mAAE↓
BEVDet4D [14]	Swin-B	56.9	45.1	0.511	0.241	0.386	0.301	0.121
PolarFormer [19]	V2-99	57.2	49.3	0.556	0.256	0.364	0.439	0.127
PETrv2 [27]	V2-99	58.2	49.0	0.561	0.243	0.361	0.343	0.120
HoP-BEVFormer [23]	V2-99	60.3	51.7	0.501	0.245	0.346	0.362	0.105
BEVDepth [13]	ConvNeXt-B	60.9	52.0	0.445	0.243	0.352	0.347	0.127
BEVStereo [15]	V2-99	61.0	52.5	0.431	0.246	0.358	0.357	0.138
SOLOFusion [16]	ConvNeXt-B	61.9	54.0	0.453	0.257	0.376	0.276	0.148
AeDet [17]	ConvNeXt-B	62.0	53.1	0.439	0.247	0.344	0.292	0.130
BEVFormerv2 [21]	InternImage-B	62.0	54.0	0.488	0.251	0.335	0.302	0.122
FB-BEV [74]	V2-99	62.4	53.7	0.439	0.250	0.358	0.270	0.128
StreamPETR [31]	V2-99	63.6	55.0	0.479	0.239	0.317	0.241	0.119
SparseBEV [32]	V2-99	63.6	55.6	0.485	0.244	0.332	0.246	0.117
Sparse4Dv2 [30]	V2-99	63.8	55.6	0.462	0.238	0.328	0.264	0.115
HENet	V2-99 & ResNet50	63.8	57.5	0.432	0.242	0.368	0.320	0.129
BEVFormerV2 [21]	InternImage-XL	64.8	58.0	0.448	0.262	0.342	0.238	0.128
BEVDet-Gamma [12] ‡	Swin-B	66.4	58.6	0.375	0.243	0.377	0.174	0.123
SparseBEV [32]	V2-99	67.5	60.3	0.425	0.239	0.311	0.172	0.116
StreamPETR-Large [31]	ViT-L	67.6	62.0	0.470	0.241	0.258	0.236	0.134
Hop [23]	ViT-L	68.5	62.4	0.367	0.249	0.353	0.171	0.131
Far3D [33]	ViT-L	68.7	63.5	0.432	0.237	0.278	0.227	0.130
HENet++	ViT-L & V2-99	70.7	64.5	0.402	0.235	0.237	0.155	0.129

each using the same settings as the multi-task model. They were all trained on the nuScenes training set for 12 epochs without CBGS. The only exception is the large detection model on the nuScenes test leaderboard, which employs 8-frame ViT-L and 15-frame VovNet-99.

The HENet++ end-to-end autonomous driving model retained the top 200 detection results and downsampled the voxels to $50 \times 50 \times 4$. We set the number of transformer layers $N = 3$. After adding the Prediction & Planning Decoder to the HENet++ perception model, this end-to-end

Table 5: Comparison of BEV semantic segmentation results on nuScenes val set. The best and second best results are marked in red and blue. For both the HENet and the HENet++ framework, the BEV Segmentation single-task models are identical.

Methods	Backbone	mIoU \uparrow	mIoU _{veh} \uparrow	mIoU _{area} \uparrow	mIoU _{div} \uparrow
VPN [39]	ResNet50	42.7	31.8	76.9	19.4
LSS [34]	ResNet50	46.5	41.7	77.7	20.0
BEVFormer [20]	ResNet101-DCN	50.2	44.8	80.1	25.7
FIERY [36]	ResNet-101	-	38.2	-	-
M2BEV [40]	ResNeXt-101	-	-	77.2	40.5
PETrv2 [27]	V2-99	60.3	46.3	85.6	49.0
HENet/HENet++	V2-99 & ResNet50	58.8	51.6	82.3	42.4

Table 6: Comparison of Occupancy results on the nuScenes-Occ3D benchmark. We present the mean IoU over categories and the IoUs for different classes. The best and second best results are marked in red and blue.

Method	Backbone	Visible Mask	mIoU \uparrow																	
				others	barrier	bicycle	bus	car	const. veh.	motorcycle	pedestrian	traffic cone	trailer	truck	drive. suf.	other flat	sidewalk	terrain	manmade	vegetation
TPVFormer [44]	R-50	✓	34.2	7.7	44.0	17.7	40.9	47.0	15.1	20.5	24.7	24.7	24.3	29.3	79.3	40.7	48.5	49.4	32.6	29.8
SurroundOcc [45]	R-101	✓	37.1	9.0	46.3	17.1	46.5	52.0	20.1	21.5	23.5	18.7	31.5	37.6	81.9	41.6	50.8	53.9	42.9	37.2
OccFormer [76]	R-50	✓	37.4	9.2	45.8	18.2	42.8	50.3	24.0	20.8	22.9	21.0	31.9	38.1	80.1	38.2	50.8	54.3	46.4	40.2
VoxFormer [46]	R-101	✓	40.7	-	-	-	-	-	-	-	-	-	-	-	-	-	-	-	-	-
FBOcc [74]	R-50	✓	42.1	14.3	49.7	30.0	46.6	51.5	29.3	29.1	29.4	30.5	35.0	39.4	83.1	47.2	55.6	59.9	44.9	39.6
PanoOcc [77]	R-101	-	42.1	11.7	50.5	29.6	49.4	55.5	23.3	33.3	30.6	31.0	34.4	42.6	83.3	44.2	54.4	56.0	45.9	40.4
FastOcc [52]	R-101	✓	40.8	12.9	46.6	29.9	46.1	54.1	23.7	31.1	30.7	28.5	33.1	39.7	83.3	44.7	53.9	55.5	42.6	36.5
BEVDet4D [14]	Swin-B	✓	42.5	12.4	50.2	27.0	51.9	54.7	28.4	29.0	29.0	28.3	37.1	42.5	82.6	43.2	54.9	58.3	48.8	43.8
FlashOcc [47]	Swin-B	✓	43.5	13.3	51.6	28.1	50.9	55.7	27.5	31.1	30.0	29.2	38.9	43.7	83.9	45.6	56.3	59.0	50.6	44.6
COTR [53]	Swin-B	✓	46.2	14.9	53.3	35.2	50.8	57.3	35.4	34.1	33.5	37.1	39.0	45.0	84.5	48.7	57.6	61.1	51.6	46.7
HENet++	R-50	✓	42.9	10.8	50.3	24.3	49.0	57.3	29.4	24.4	30.1	28.5	36.5	43.0	84.0	43.1	56.0	59.3	54.2	49.2
HENet++	V2-99 & R-50	✓	48.2	13.7	58.2	28.6	57.7	60.8	34.0	33.4	39.9	34.1	46.8	52.1	84.4	46.7	58.3	61.6	58.6	51.0

autonomous driving model was fine-tuned for 10 epochs (without CBGS).

6.2 Dataset and Metrics

We evaluate our model on the nuScenes [78] dataset, a large-scale autonomous driving dataset containing 1,000 driving scenes (700 for training, 150 for validation, and 150 for testing), including cities, highways, and rural roads. Each scene contains various objects, such as vehicles, pedestrians, and bicycles.

For 3D object detection evaluation, NuScenes provides a set of evaluation metrics, including mean Average Precision (mAP) and five true positive (TP) metrics: ATE, ASE, AOE, AVE, and AAE for measuring translation, scale, orientation, velocity, and attribute errors, respectively. The overall performance is measured by the nuScenes Detection Score (NDS), which is the composite

of the above metrics. For BEV semantic segmentation, we use mean intersection over union (mIoU) as the metric following the settings of LSS [34]. For Occupancy, we use IoU to evaluate binary occupancy results, i.e., whether a voxel is occupied regardless of its semantic category. Additionally, we use mIoU, the class-averaged IoU metric, to evaluate semantic occupancy predictions. For End-to-end Autonomous Driving, commonly used evaluation metrics include the L2 distance to expert human trajectories and the collision rate. Models like UniAD [57] and VAD [58]/STP3 [56] adopt different benchmarks, for instance, whether to average over time and which object categories are counted as collisions. We have conducted evaluations on both benchmarks.

Table 7: Ablation of Hybrid Image Encoding Network on Detection Task. ‘Time’ denotes the overall training time. ‘BS’ indicates the batch size. For A \bar{F} , FPS is measured on RTX3090 GPU with FP32. For H \bar{I} , FPS is measured on A100-SMX4 GPU with FP32 and FP16 mixed precision. For A \bar{F} , Training cost (GPU memory and Time) is estimated on 8×Tesla A800 GPUs with FP32. For H \bar{I} , Training cost is estimated on 8×A100-SMX4 GPUs with FP32 and FP16 mixed precision.

	Model	Backbone	Input	Frames	NDS	mAP	FPS	GPU memory	Time
A	BEVDepth4D	R18	640×1152	2 frames	48.6	34.8	14.3	31.2G / BS=64	14h
B	BEVDepth4D	R18	256×704	9 frames	48.6	34.9	21.7	22.9G / BS=64	14h
C	BEVDepth4D	R18	640×1152	9 frames	51.2	39.2	14.1	43.5G / BS=64	44h
A+B	Model Ensemble	-	-	-	48.9	35.2	7.93	-	-
A+B	HENet	R18 & R18	640×1152 & 256×704	2 + 7 frames	52.1	39.8	8.91	41.3G / BS=64	13h
D	BEVDepth4D	R50	256×704	9 frames	53.8	40.9	19.1	14.1G / BS=16	16h
E	BEVStereo	V2-99	640×1152	2 frames	58.2	48.0	4.52	37.0G / BS=16	48h
F	BEVStereo	V2-99	896×1600	2 frames	59.2	50.0	2.69	68.4G / BS=16	96h
D+E	Model Ensemble	-	-	-	57.3	46.4	3.53	-	-
D+E	HENet w/o AFFM	V2-99 & R50	640×1152 & 256×704	2 + 7 frames	59.2	49.9	3.71	42.3G / BS=16	27h
D+E	HENet	V2-99 & R50	640×1152 & 256×704	2 + 7 frames	59.9	50.2	3.65	43.5G / BS=16	27h
H	SparseBEV	R50	256×704	11 frames	55.8	45.2	31.1	14.7G / BS=8	17h
I	SparseBEV	V2-99	640×1600	8 frames	63.2	55.1	9.6	70.4G / BS=8	100h
H+I	Model Ensemble	-	-	11 frames	60.8	52.7	7.3	-	-
H+I	HENet++	V2-99 & R50	640×1600 & 256×704	5 + 6 frames	65.1	57.3	12.1	68.9G / BS=8	72h

6.3 Multi-task Results

We compare the proposed HENet and HENet++ with previous end-to-end multi-task models on the nuScenes val sets in Table 1 and Figure 1. HENet++ shows favorable multi-task performance and achieves state-of-the-art results. Specifically, HENet++ outperforms BEVFormer [20] by 11.0 NDS and 15.5 mAP on the 3D object detection task, 8.9 mIoU on the BEV semantic segmentation task, and 15.9 mIoU on the Occupancy task. As for PETRv2 [27], which shows excellent BEV semantic segmentation performance, our models surpass it by 14.2 NDS on the 3D object detection task while maintaining competitive BEV semantic segmentation performance. In addition, we compare the training time per epoch (with the same batch size) with these methods. HENet outperforms all other methods with less training time, showing the proposed HENet is more efficient. Moreover, HENet can use more frames to improve performance, while other methods, like PETRv2, cannot use 9 frames due to the limitation of GPU memory.

We also compare the results of HENet++ for end-to-end autonomous driving with other end-to-end autonomous driving methods in Table 2. Although HENet++ exhibits a higher L2 error compared to human driving trajectories, this does not imply a higher planning error rate, as

it achieves a lower collision rate than existing method.

6.4 Single Task Results

Considering that many works on 3D perception only predict single-task results, we conduct experiments on single tasks and compare the results of HENet with these task-specific models. Through this comparison, we illustrate the superiority of our Hybrid Image Encoding Network and Temporal Feature Integration, and further demonstrate the effectiveness of HENet.

3D Object Detection Results. We present the results of HENet and HENet++ for single 3D object detection task on the nuScenes val and test sets in Table 3 and 4, respectively. As shown in Table 3, HENet and HENet++ surpasses all multi-view camera 3D object detection methods under different backbone configurations, demonstrating the effectiveness of the proposed hybrid image encoding network and temporal feature integration module. Table 4 shows HENet++ achieves state-of-the-art 3D object detection results. By transitioning from the BEV paradigm to the sparse paradigm, HENet++ achieves better 3D object detection results than HENet. Meanwhile, when comparing HENet++ with its primary baseline SparseBEV, the results demonstrate that Hybrid Encoding can effectively improve performance.

Table 8: Ablation of Hybrid Image Encoding Network on Multi-task. $mIoU_{bev}$ and $mIoU_{occ}$ denote the mIoU for BEV semantic segmentation and semantic occupancy, respectively.

	Model	Backbone	Input	Frames	NDS	$mIoU_{bev}$	$mIoU_{occ}$
A	BEVDepth4D	R50	256×704	9 frames	53.0	51.5	-
B	BEVStereo	V2-99	640×1152	2 frames	58.0	55.8	-
C	BEVStereo	V2-99	896×1600	2 frames	58.9	56.7	-
A+B	HENet w/o AFFM	V2-99 & R50	640×1152 & 256×704	2 + 7 frames	59.0	56.9	-
A+B	HENet w/ AFFM	V2-99 & R50	640×1152 & 256×704	2 + 7 frames	59.9	58.0	-
D	HENet++ w/o HE	R50	256×704	9 frames	54.1	51.9	39.4
E	HENet++ w/o HE	V2-99	640×1600	8 frames	63.0	58.1	45.5
D+E	HENet++	V2-99 & R50	640×1600 & 256×704	5 + 6 frames	63.7	58.3	47.3



Fig. 9: Visualization results of HENet and baselines on end-to-end multi-tasking. From left to right, we show multi-view image inputs, results of BEVDepth4D, BEVStereo, and HENet (BEVDepth4D + BEVStereo), and the ground truth. The proposed HENet estimates occluded objects better through long-term information and has more accurate predictions through high-resolution information.

BEV Semantic Segmentation Results.

We present the results of HENet for single BEV semantic segmentation task on the nuScenes val sets in Table 5. HENet obtain competitive results compared to existing methods. In the HENet++ framework, BEV semantic segmentation is still decoded from dense features, and the design of the BEV segmentation single-task model remains identical. Therefore, the results for HENet and HENet++ are presented in the same row in Table 5.

Occupancy Results. We present the results of HENet++ for single BEV semantic segmentation task on the nuScenes val sets in Table 6. HENet++ obtains state-of-the-art results.

It is worth mentioning that compared with single-task performance, the end-to-end multi-task performance of HENet++ only drops 0.6 mAP

for the 3D object detection task, 0.5 mIoU for the BEV semantic segmentation task, and 0.9 mIoU for the Occupancy task, respectively.

6.5 Ablation Study

We also conduct ablation studies for each proposed module on nuScenes val set.

Hybrid Image Encoding Network. To demonstrate the effectiveness of the proposed hybrid image encoding network, we compare HENet and HENet++ with three baseline methods and their ensemble model. As shown in Table 7, by combining with BEVDepth4D [13] and BEVStereo [15] through hybrid image encoding, HENet can significantly improve the 3D object detection performance. Compared to increasing resolution (model C), Hybrid Image Encoding Network can achieve higher accuracy with faster

Table 9: Ablation of Temporal Feature Integration module of HENet. Our proposed backward and forward processes with AFFM achieve the best results.

Temporal Integration	NDS	mAP	Parameters
Global Concatenation&Conv (BEVDepth4D [14])	52.3	40.8	76.51M
Global Concatenation&Conv + larger BEV encoder	52.4	40.7	77.70M
Global attention	52.6	40.9	76.68M
Forward with adjacent Concatenation&Conv	52.8	40.6	76.63M
Forward with AFFM	53.1	41.2	76.64M
Backward + Forward with adjacent Concatenation&Conv	52.8	40.7	76.63M
Backward + Forward with AFFM (Ours)	53.2	41.5	76.64M

Table 10: Ablation of Independent BEV Feature Encoding of HENet. ‘AFS’ is the adaptive feature selection. ‘IE’ denotes the independent BEV encoder. All experiments only used a single BEVDepth4D with ResNet-50 as the image encoder.

Det-grid	Seg-grid	AFS	IE	NDS	mAP	mIoU			
0.4m	0.4m			53.2	41.9	41.6			
0.8m	0.8m			50.5	39.6	50.9			
0.4m	0.8m			52.9	42.0	50.6			
0.4m	0.8m	✓		53.3	↑0.4	42.3	↑0.3	51.2	↑0.6
0.4m	0.8m	✓	✓	54.6	↑1.7	43.1	↑1.1	54.0	↑3.4

Table 11: Ablation of Pretrain Method of HENet++. This experiment is conducted on a triple-task R50 small model. Compared to using single-task detection or occupancy weights, loading the merged model for pre-training improves multi-task performance.

Load from	NDS	mIoU _{bev}	mIoU _{occ}
Detection	53.7	54.6	36.2
Occupancy	53.2	55.2	37.4
Model Merge	53.9	55.3	37.5

Table 12: Ablation on the Loss for End-to-End Autonomous Driving.

\mathcal{L}_{plan}	\mathcal{L}_{pred}	\mathcal{L}_{col}	UniAD Metrics		VAD/STP3 Metrics	
			mean L2	mean Col.	mean L2	mean Col.
✓			1.69	0.52	0.71	0.17
✓	✓		1.36	0.20	0.58	0.10
✓	✓	✓	1.29	0.13	0.55	0.05

inference speed and lower training costs. Compared to increasing the frame number (model F), Hybrid Image Encoding Network can achieve higher accuracy with lower training costs. Notably, ensembling the results of the two baselines by NMS decreases the overall performance since the weaker BEVDepth4D [13] introduces many false

positive detection results. The same conclusion can be drawn from the comparative experiments between SparseBEV [32] and HENet++, thereby demonstrating that Hybrid Encoding is effective across both BEV-based and sparse-feature-based perception frameworks.

For better comparison, we provide a multi-task ablation study, as shown in Table 8.

We also provide the visualization of the detection results in Figure 9. It can be seen that, due to motion or occlusion, some objects or scenes (as shown in the blue boxes) require a longer time sequence. Besides, high-resolution and sophisticated depth estimation methods benefit the perception of difficult objects and scenes (as shown in the red boxes). HENet and HENet++ can effectively combine the advantages of long-time sequence, high-resolution, and sophisticated depth estimation.

Temporal Feature Integration of HENet.

Table 9 compares the results between different types of temporal feature integration methods.

Our adjacent attention achieves the best results.

We observe that adjacent design is more effective than global operation, whether using attention or using Concatenation&Conv. Besides, compared to concatenation and convolution, our AFFM, which is based on the attention mechanism, performs better. Lastly, global attention and the larger BEV encoder introduce more model parameters and achieve worse performance than pair-wise attention. This demonstrates that the performance improvements in pairwise attention stem from the design itself rather than from increased model parameters.

Independent BEV Feature Encoding of HENet. As analyzed in [66], 3D object detection and BEV semantic segmentation tasks prefer different BEV feature grid sizes. As shown in

Table 10, using BEV feature maps of different sizes across tasks achieves the best trade-off in multi-task performance. Moreover, adopting independent adaptive feature selection and BEV encoder for each task can further improve the multi-task performance of 1.7 NDS, 1.1 mAP, and 3.4 mIoU.

Pretrain with Model Merge of HENet++. As shown in Figure 11, compared to using single-task detection or occupancy weights, loading the merged model for pre-training improves multi-task performance.

Loss for End-to-End Autonomous Driving of HENet++. The experimental results in Figure 12 demonstrate the effectiveness of the loss mentioned in Section 5.

7 Conclusion

In this paper, we first present HENet, an end-to-end framework for multi-task 3D perception. We propose a Hybrid Image Encoding Network for BEV and a Temporal Feature Integration Module to handle high-resolution, long-term temporal image inputs efficiently. Besides, we adopt task-specific BEV grid sizes, an Independent BEV Feature Encoder and Decoder to address the multi-task conflict issue.

Based on further analysis of the characteristics of different tasks in existing work, we introduce the HENet++ framework. By simultaneously hybrid encoding for sparse foreground features and dense background voxel features, the framework enables end-to-end prediction for 3D object detection, BEV semantic segmentation, and occupancy semantic segmentation, providing suitable features for each task. In addition, we introduce a model-merging-based pre-training strategy that further enhances multi-task performance. HENet++ achieves state-of-the-art end-to-end multi-task perception performance on the nuScenes dataset.

Based on the HENet++ perception framework, we further design an end-to-end autonomous driving model. Leveraging the extracted sparse foreground features and dense background features, HENet++ employs an attention-based world-prediction module to perform prediction and ego-vehicle trajectory planning simultaneously. HENet++ is the first work that leverages Radar and Camera for end-to-end autonomous driving. On the nuScenes dataset, the HENet++ model

achieves a lower collision rate compared to existing methods.

Declarations

Preliminary Version. A preliminary version of this manuscript was published in [66].

Acknowledgements. This work was supported by National Key R&D Program of China (Grant No. 2022ZD0160305) and National Natural Science Foundation of China (Grant No. 62176007).

Data Availability. All experiments are conducted on publicly available datasets. To be specific, the nuScenes dataset is available at <https://www.nuscenes.org/nuscenes>. The Occupancy Ground Truth of nuScenes can be found at <https://github.com/Tsinghua-MARS-Lab/Occ3D>.

References

- [1] Weng, X., Ivanovic, B., Wang, Y., Wang, Y., Pavone, M.: Para-drive: Parallelized architecture for real-time autonomous driving. In: CVPR, pp. 15449–15458 (2024)
- [2] Zheng, W., Song, R., Guo, X., Chen, L.: Genad: Generative end-to-end autonomous driving. In: ECCV (2024)
- [3] Sun, W., Lin, X., Shi, Y., Zhang, C., Wu, H., Zheng, S.: Sparsedrive: End-to-end autonomous driving via sparse scene representation. In: ICRA (2025)
- [4] Wang, Y., Chao, W.-L., Garg, D., Hariharan, B., Campbell, M., Weinberger, K.Q.: Pseudolidar from visual depth estimation: Bridging the gap in 3d object detection for autonomous driving. In: CVPR, pp. 8445–8453 (2019)
- [5] Wang, T., Zhu, X., Pang, J., Lin, D.: Fcos3d: Fully convolutional one-stage monocular 3d object detection. In: ICCV (2021)
- [6] Ding, M., Huo, Y., Yi, H., Wang, Z., Shi, J., Lu, Z., Luo, P.: Learning depth-guided convolutions for monocular 3d object detection. In: CVPR (2020)

- [7] Brazil, G., Liu, X.: M3d-rpn: Monocular 3d region proposal network for object detection. In: ICCV (2019)
- [8] Wang, T., Pang, J., Lin, D.: Monocular 3d object detection with depth from motion. In: ECCV (2022)
- [9] Park, D., Ambrus, R., Guizilini, V., Li, J., Gaidon, A.: Is pseudo-lidar needed for monocular 3d object detection? In: ICCV (2021)
- [10] Reading, C., Harakeh, A., Chae, J., Waslander, S.L.: Categorical depth distribution network for monocular 3d object detection. In: CVPR, pp. 8555–8564 (2021)
- [11] Roddick, T., Kendall, A., Cipolla, R.: Orthographic feature transform for monocular 3d object detection. arXiv preprint arXiv:1811.08188 (2018)
- [12] Huang, J., Huang, G., Zhu, Z., Ye, Y., Du, D.: Bevdet: High-performance multi-camera 3d object detection in bird-eye-view. arXiv preprint arXiv:2112.11790 (2021)
- [13] Li, Y., Ge, Z., Yu, G., Yang, J., Wang, Z., Shi, Y., Sun, J., Li, Z.: Bevdepth: Acquisition of reliable depth for multi-view 3d object detection. In: AAAI (2023)
- [14] Huang, J., Huang, G., Robotics, P.: Bevdet4d: Exploit temporal cues in multi-camera 3d object detection. arXiv preprint arXiv:2203.17054 (2022)
- [15] Li, Y., Bao, H., Ge, Z., Yang, J., Sun, J., Li, Z.: Bevstereo: Enhancing depth estimation in multi-view 3d object detection with dynamic temporal stereo. In: AAAI (2023)
- [16] Park, J., Xu, C., Yang, S., Keutzer, K., Kitani, K., Tomizuka, M., Zhan, W.: Time will tell: New outlooks and a baseline for temporal multi-view 3d object detection. In: ICLR (2023)
- [17] Feng, C., Jie, Z., Zhong, Y., Chu, X., Ma, L.: Aedet: Azimuth-invariant multi-view 3d object detection. In: CVPR, pp. 21580–21588 (2023)
- [18] Huang, B., Li, Y., Xie, E., Liang, F., Wang, L., Shen, M., Liu, F., Wang, T., Luo, P., Shao, J.: Fast-bev: Towards real-time on-vehicle bird’s-eye view perception. arXiv preprint arXiv:2301.07870 (2023)
- [19] Jiang, Y., Zhang, L., Miao, Z., Zhu, X., Gao, J., Hu, W., Jiang, Y.-G.: Polarformer: Multi-camera 3d object detection with polar transformer. In: AAAI, pp. 1042–1050 (2023)
- [20] Li, Z., Wang, W., Li, H., Xie, E., Sima, C., Lu, T., Qiao, Y., Dai, J.: Bevformer: Learning bird’s-eye-view representation from multi-camera images via spatiotemporal transformers. In: ECCV (2022)
- [21] Yang, C., Chen, Y., Tian, H., Tao, C., Zhu, X., Zhang, Z., Huang, G., Li, H., Qiao, Y., Lu, L., *et al.*: Bevformer v2: Adapting modern image backbones to bird’s-eye-view recognition via perspective supervision. In: CVPR, pp. 17830–17839 (2023)
- [22] Wang, Z., Min, C., Ge, Z., Li, Y., Li, Z., Yang, H., Huang, D.: Sts: Surround-view temporal stereo for multi-view 3d detection. arXiv preprint arXiv:2208.10145 (2022)
- [23] Zong, Z., Jiang, D., Song, G., Xue, Z., Su, J., Li, H., Liu, Y.: Temporal enhanced training of multi-view 3d object detector via historical object prediction. In: ICCV (2023)
- [24] Zhang, Y., Zheng, W., Zhu, Z., Huang, G., Lu, J., Zhou, J.: A simple baseline for multi-camera 3d object detection. In: AAAI, pp. 3507–3515 (2023)
- [25] Wang, Y., Guizilini, V., Zhang, T., Wang, Y., Zhao, H., Solomon, J.: Detr3d: 3d object detection from multi-view images via 3d-to-2d queries. In: CoRL (2021)
- [26] Liu, Y., Wang, T., Zhang, X., Sun, J.: Petr: Position embedding transformation for multi-view 3d object detection. In: ECCV (2022)
- [27] Liu, Y., Yan, J., Jia, F., Li, S., Gao, A., Wang, T., Zhang, X.: Petr v2: A unified framework for 3d perception from multi-camera images. In: ICCV (2023)

- [28] Yang, Z., Zhou, Y., Chen, Z., Ngiam, J.: 3d-man: 3d multi-frame attention network for object detection. In: CVPR, pp. 1863–1872 (2021)
- [29] Lin, X., Lin, T., Pei, Z., Huang, L., Su, Z.: Sparse4d: Multi-view 3d object detection with sparse spatial-temporal fusion. arXiv preprint arXiv:2211.10581 (2022)
- [30] Lin, X., Lin, T., Pei, Z., Huang, L., Su, Z.: Sparse4d v2: Recurrent temporal fusion with sparse model. arXiv preprint arXiv:2305.14018 (2023)
- [31] Wang, S., Liu, Y., Wang, T., Li, Y., Zhang, X.: Exploring object-centric temporal modeling for efficient multi-view 3d object detection. In: ICCV (2023)
- [32] Liu, H., Teng, Y., Lu, T., Wang, H., Wang, L.: Sparsebev: High-performance sparse 3d object detection from multi-camera videos. In: ICCV (2023)
- [33] Jiang, X., Li, S., Liu, Y., Wang, S., Jia, F., Wang, T., Han, L., Zhang, X.: Far3d: Expanding the horizon for surround-view 3d object detection. In: AAAI (2024)
- [34] Pillion, J., Fidler, S.: Lift, splat, shoot: Encoding images from arbitrary camera rigs by implicitly unprojecting to 3d. In: ECCV (2020)
- [35] Nicolas, C., Francisco, M., Gabriel, S., Nicolas, U., Alexander, K., Sergey, Z.: End-to-end object detection with transformers. In: ECCV (2020)
- [36] Hu, A., Murez, Z., Mohan, N., Dudas, S., Hawke, J., Badrinarayanan, V., Cipolla, R., Kendall, A.: Fiery: Future instance prediction in bird’s-eye view from surround monocular cameras. In: ICCV (2021)
- [37] Yang, W., Li, Q., Liu, W., Yu, Y., Ma, Y., He, S., Pan, J.: Projecting your view attentively: Monocular road scene layout estimation via cross-view transformation. In: CVPR (2021)
- [38] Roddick, T., Cipolla, R.: Predicting semantic map representations from images using pyramid occupancy networks. In: CVPR (2020)
- [39] Pan, B., Sun, J., Leung, H.Y.T., Andonian, A., Zhou, B.: Cross-view semantic segmentation for sensing surroundings. IEEE Robotics and Automation Letters (2020)
- [40] Xie, E., Yu, Z., Zhou, D., Pillion, J., Anandkumar, A., Fidler, S., Luo, P., Alvarez, J.M.: M2bev: Multi-camera joint 3d detection and segmentation with unified birds-eye view representation. arXiv preprint arXiv:2204.05088 (2022)
- [41] Zhou, B., Krähenbühl, P.: Cross-view transformers for real-time map-view semantic segmentation. In: CVPR (2022)
- [42] Li, Q., Wang, Y., Wang, Y., Zhao, H.: Hdmapnet: An online hd map construction and evaluation framework. In: ICRA (2022)
- [43] Cao, A.-Q., De Charette, R.: Monoscene: Monocular 3d semantic scene completion. In: CVPR, pp. 3991–4001 (2022)
- [44] Huang, Y., Zheng, W., Zhang, Y., Zhou, J., Lu, J.: Tri-perspective view for vision-based 3d semantic occupancy prediction. In: CVPR, pp. 9223–9232 (2023)
- [45] Wei, Y., Zhao, L., Zheng, W., Zhu, Z., Zhou, J., Lu, J.: Surroundocc: Multi-camera 3d occupancy prediction for autonomous driving. In: ICCV, pp. 21729–21740 (2023)
- [46] Li, Y., Yu, Z., Choy, C., Xiao, C., Alvarez, J.M., Fidler, S., Feng, C., Anandkumar, A.: Voxformer: Sparse voxel transformer for camera-based 3d semantic scene completion. In: CVPR, pp. 9087–9098 (2023)
- [47] Yu, Z., Shu, C., Deng, J., Lu, K., Liu, Z., Yu, J., Yang, D., Li, H., Chen, Y.: Flashocc: Fast and memory-efficient occupancy prediction via channel-to-height plugin. arXiv preprint arXiv:2311.12058 (2023)
- [48] Li, Z., Yu, Z., Austin, D., Fang, M., Lan, S., Kautz, J., Alvarez, J.M.: Fb-occ: 3d

- occupancy prediction based on forward-backward view transformation. arXiv preprint arXiv:2307.01492 (2023)
- [49] Pan, M., Liu, L., Liu, J., Huang, P., Wang, L., Zhang, S., Xu, S., Lai, Z., Yang, K.: Uniocc: Unifying vision-centric 3d occupancy prediction with geometric and semantic rendering. arXiv preprint arXiv:2306.09117 (2023)
- [50] Pan, M., Liu, J., Zhang, R., Huang, P., Li, X., Liu, L., Zhang, S.: Renderocc: Vision-centric 3d occupancy prediction with 2d rendering supervision. arXiv preprint arXiv:2309.09502 (2023)
- [51] Wang, Z., Wu, S., Xie, W., Chen, M., Prisacariu, V.A.: Nerf-: Neural radiance fields without known camera parameters. arXiv preprint arXiv:2102.07064 (2021)
- [52] Hou, J., Li, X., Guan, W., Zhang, G., Feng, D., Du, Y., Xue, X., Pu, J.: Fastocc: Accelerating 3d occupancy prediction by fusing the 2d bird’s-eye view and perspective view. arXiv preprint arXiv:2403.02710 (2024)
- [53] Ma, Q., Tan, X., Qu, Y., Ma, L., Zhang, Z., Xie, Y.: Cotr: Compact occupancy transformer for vision-based 3d occupancy prediction. In: CVPR, pp. 19936–19945 (2024)
- [54] Zhuang, Z., Li, R., Jia, K., Wang, Q., Li, Y., Tan, M.: Perception-aware multi-sensor fusion for 3d lidar semantic segmentation. In: ICCV (2021)
- [55] Yuan, Y., Huang, L., Guo, J., Zhang, C., Chen, X., Wang, J.: Ocnet: Object context network for scene parsing. arXiv preprint arXiv:1809.00916 (2018)
- [56] Hu, S., Chen, L., Wu, P., Li, H., Yan, J., Tao, D.: St-p3: End-to-end vision-based autonomous driving via spatial-temporal feature learning. In: ECCV, pp. 533–549 (2022). Springer
- [57] Hu, Y., Yang, J., Chen, L., Li, K., Sima, C., Zhu, X., Chai, S., Du, S., Lin, T., Wang, W., Lu, L., Jia, X., Liu, Q., Dai, J., Qiao, Y., Li, H.: Planning-oriented autonomous driving. In: CVPR (2023)
- [58] Jiang, B., Chen, S., Xu, Q., Liao, B., Chen, J., Zhou, H., Zhang, Q., Liu, W., Huang, C., Wang, X.: Vad: Vectorized scene representation for efficient autonomous driving. In: ICCV, pp. 8340–8350 (2023)
- [59] Song, Z., Jia, C., Liu, L., Pan, H., Zhang, Y., Wang, J., Zhang, X., Xu, S., Yang, L., Luo, Y.: Don’t shake the wheel: Momentum-aware planning in end-to-end autonomous driving. In: CVPR (2025)
- [60] Zhang, B., Song, N., Jin, X., Zhang, L.: Bridging past and future: End-to-end autonomous driving with historical prediction and planning. In: CVPR (2025)
- [61] Liao, B., Chen, S., Yin, H., Jiang, B., Wang, C., Yan, S., Zhang, X., Li, X., Zhang, Y., Zhang, Q., *et al.*: Diffusiondrive: Truncated diffusion model for end-to-end autonomous driving. In: CVPR (2025)
- [62] Lee, Y., Park, J.: Centermask: Real-time anchor-free instance segmentation. In: CVPR (2020)
- [63] Lin, T.-Y., Dollár, P., Girshick, R., He, K., Hariharan, B., Belongie, S.: Feature pyramid networks for object detection. In: CVPR (2017)
- [64] He, K., Zhang, X., Ren, S., Sun, J.: Deep residual learning for image recognition. In: CVPR (2016)
- [65] Huang, J., Huang, G.: Bevpoolv2: A cutting-edge implementation of bevdet toward deployment. arXiv preprint arXiv:2211.17111 (2022)
- [66] Xia, Z., Lin, Z., Wang, X., Wang, Y., Xing, Y., Qi, S., Dong, N., Yang, M.-H.: Henet: Hybrid encoding for end-to-end multi-task 3d perception from multi-view cameras. In: ECCV (2024)
- [67] Liang, T., Xie, H., Yu, K., Xia, Z., Lin, Z., Wang, Y., Tang, T., Wang, B., Tang, Z.: Bevfusion: A simple and robust lidar-camera fusion framework. In: NeurIPS (2022)

- [68] Yin, T., Zhou, X., Krahenbuhl, P.: Center-based 3d object detection and tracking. In: CVPR (2021) CVPR (2020)
- [69] Badrinarayanan, V., Kendall, A., Cipolla, R.: Segnet: A deep convolutional encoder-decoder architecture for image segmentation. *IEEE TPAMI* (2017)
- [70] Jin, X., Ren, X., Preotiuc-Pietro, D., Cheng, P.: Dataless knowledge fusion by merging weights of language models. In: *ICLR* (2023)
- [71] Lin, Z., Liu, Z., Wang, Y., Zhang, L., Zhu, C.: Rcbvdet++: toward high-accuracy radar-camera fusion 3d perception network. *arXiv preprint arXiv:2409.04979* (2024)
- [72] Tong, W., Sima, C., Wang, T., Chen, L., Wu, S., Deng, H., Gu, Y., Lu, L., Luo, P., Lin, D., *et al.*: Scene as occupancy. In: *ICCV*, pp. 8406–8415 (2023)
- [73] Li, P., Cui, D.: Navigation-guided sparse scene representation for end-to-end autonomous driving. In: *ICLR* (2025)
- [74] Li, Z., Yu, Z., Wang, W., Anandkumar, A., Lu, T., Alvarez, J.M.: Fb-bev: Bev representation from forward-backward view transformations. In: *ICCV*, pp. 6919–6928 (2023)
- [75] Zhu, B., Jiang, Z., Zhou, X., Li, Z., Yu, G.: Class-balanced grouping and sampling for point cloud 3d object detection. *arXiv preprint arXiv:1908.09492* (2019)
- [76] Zhang, Y., Zhu, Z., Du, D.: Occformer: Dual-path transformer for vision-based 3d semantic occupancy prediction. In: *ICCV*, pp. 9433–9443 (2023)
- [77] Wang, Y., Chen, Y., Liao, X., Fan, L., Zhang, Z.: Panoocc: Unified occupancy representation for camera-based 3d panoptic segmentation. In: *CVPR*, pp. 17158–17168 (2024)
- [78] Caesar, H., Bankiti, V., Lang, A.H., Vora, S., Liong, V.E., Xu, Q., Krishnan, A., Pan, Y., Baldan, G., Beijbom, O.: nusenes: A multimodal dataset for autonomous driving. In: